Magnetic resonance imaging with hyperpolarized [1,4-^{13}C$_2$]fumarate allows detection of early renal acute tubular necrosis

Menna R. Clatworthy[a,b,1], Mikko I. Kettunen[c,d,1], De-En Hu[c,d], Rebeccah J. Mathews[a], Timothy H. Witney[c,d], Brett W. C. Kennedy[c,d], Sarah E. Bohndiek[c,d], Ferdia A. Gallagher[c,d], Lorna B. Jarvis[a], Kenneth G. C. Smith[a,b,2], and Kevin M. Brindle[c,d,2,3]

[a]Cambridge Institute for Medical Research and [b]Department of Medicine, University of Cambridge School of Clinical Medicine, Addenbrooke's Hospital, Cambridge CB2 0XY, United Kingdom; [c]Department of Biochemistry, University of Cambridge, CB2 1GA Cambridge, United Kingdom; and [d]Cancer Research UK, Cambridge Research Institute, Cambridge CB2 0RE, United Kingdom

Acute kidney injury (AKI) is a common and important medical problem, affecting 10% of hospitalized patients, and it is associated with significant morbidity and mortality. The most frequent cause of AKI is acute tubular necrosis (ATN). Current imaging techniques and biomarkers do not allow ATN to be reliably differentiated from important differential diagnoses, such as acute glomerulonephritis (GN). We investigated whether ^{13}C magnetic resonance spectroscopic imaging (MRSI) might allow the noninvasive diagnosis of ATN. ^{13}C MRSI of hyperpolarized [1,4-^{13}C$_2$]fumarate and pyruvate was used in murine models of ATN and acute GN (NZM2410 mice with lupus nephritis). A significant increase in [1,4-^{13}C$_2$]malate signal was identified in the kidneys of mice with ATN early in the disease course before the onset of severe histological changes. No such increase in renal [1,4-^{13}C$_2$]malate was observed in mice with acute GN. The kidney [1-^{13}C]pyruvate/[1-^{13}C]lactate ratio showed substantial variability and was not significantly decreased in animals with ATN or increased in animals with GN. In conclusion, MRSI of hyperpolarized [1,4-^{13}C$_2$]fumarate allows the detection of early tubular necrosis and its distinction from glomerular inflammation in murine models. This technique may have the potential to identify a window of therapeutic opportunity in which emerging therapies might be applied to patients with ATN, reducing the need for acute dialysis with its attendant morbidity and cost.

hyperpolarization | MRI

The absence of a noninvasive test for early diagnosis of the cause of acute kidney injury (AKI) is a major problem in acute medical care. AKI is a common and clinically important problem, affecting 5–10% of hospitalized patients and 30–40% of those in a critical care unit (1, 2). AKI is associated with significant morbidity and mortality (10–20% in the first year postdiagnosis in patients requiring renal support) (1, 2). The most common cause of AKI, particularly in the critical care setting, is acute tubular necrosis (ATN), which results from a reduction in systemic blood pressure, exposure to toxins, or the formation of casts within tubules (3). Regardless of the cause, ATN is characterized histologically by flattening of tubular epithelium, tubular dilatation, and loss of tubular cell nuclei (4); functionally, it is characterized by loss of electrolyte handling, leading to a high urinary sodium concentration (5, 6).

One of the main differential diagnoses in patients with AKI is acute glomerulonephritis (GN), an inflammatory condition that may be primary (idiopathic) or may occur secondary to immune-mediated diseases, such as systemic lupus erythematosus. Early diagnosis is of utmost importance, because management differs radically; in ATN, renal support, removal of nephrotoxins, and maintenance of an adequate fluid balance are necessary, whereas in acute GN, immunosuppressive agents are also required.

Currently, there is no noninvasive test that reliably differentiates between ATN and acute GN. If clinical history and urine or serum analysis do not clarify the diagnosis, renal biopsy is required, which carries a risk of hemorrhage (7, 8) and is often not possible in critically ill patients.

In recent years, the development of specific therapies (9–11) has led to increasing interest in the early diagnosis of ATN and a more accurate definition and classification of AKI has been devised to facilitate clinical trials of such therapies (12, 13). In addition, there has been intense interest in the identification of biomarkers that allow the diagnosis of ATN before the development of established disease, at a stage when therapies may have an impact on progression (14, 15). Thus, diagnostic tools are required that not only allow the early identification of ATN but its distinction from other differential diagnoses, such as GN.

Diffusion-weighted MRI has proved useful in identifying ureteric or vascular obstruction but does not readily differentiate ATN from immune-mediated pathologies (16). Magnetic resonance spectroscopy (MRS) has been used to detect biochemical changes associated with disease in a variety of organs, including the kidneys (17), but it is limited by its low sensitivity (18). Hyperpolarization of ^{13}C-labeled molecules radically enhances their detection by ^{13}C-MRS (19) and has allowed metabolic imaging of several substrates in vivo (20), including fumarate and pyruvate (21–23). Fumarate, a tricarboxylic acid cycle intermediate, is hydrated to form malate by the enzyme fumarase. In viable cells, fumarate uptake is limited within the lifetime of the hyperpolarized ^{13}C label; however, in necrotic cells, where plasma membrane permeability is compromised, there is increased uptake of hyperpolarized [1,4-^{13}C$_2$]fumarate and production of hyperpolarized [1,4-^{13}C$_2$]malate (22). This has been demonstrated following chemotherapy-induced necrosis in tumor cells in vitro and in implanted tumors in vivo (22, 23). Pyruvate, a product of glycolysis, is reduced to lactate by NADH in the reaction catalyzed by lactate dehydrogenase (LDH). Following injection of

hyperpolarized [1-^{13}C]pyruvate into tumor-bearing animals, there is significant exchange of hyperpolarized ^{13}C label between the injected pyruvate and the endogenous tumor lactate pool. Decreases in this exchange have been used to detect early evidence of tumor responses to treatment, where this was shown to be attributable to a number of factors, including tumor cell necrosis, with an attendant loss of LDH activity (21). Of note, LDH lost from tubular cells is detectable in the urine in patients with ATN (24, 25). In contrast, in a rodent arthritis model, there was an increase in [1-^{13}C]lactate signal in inflamed tissues (26).

Given the potential of both hyperpolarized [1,4-^{13}C$_2$]fumarate and [1-^{13}C]pyruvate for detecting necrosis and of [1-^{13}C]pyruvate for detecting inflammation, we sought to determine whether these hyperpolarized substrates could be used to detect necrosis in renal tubular cells and to distinguish this from the inflammation associated with acute GN. We used rodent models of ATN [folic acid (FA)-induced nephropathy (27)] and GN [lupus nephritis in the New Zealand mixed (NZM) 2410 congenic strain (28)]. FA-induced ATN results in histological changes that are common to all murine models of ATN and are identical to those observed in human disease, that is, flattening of tubular epithelium, with loss of tubular nuclei, particularly affecting tubules at the corticomedullary junction. The disease course is also similar to that seen in humans, in that some animals spontaneously recover renal function over a period of days, whereas others succumb to renal failure. ATN in this model is accompanied by proteinuria, which is not usually as prominent in human ATN, although tubular proteinuria has been investigated for its clinical potential as a marker of tubular damage in human AKI (25). We demonstrate that administration of hyperpolarized [1,4-^{13}C$_2$]fumarate in these murine models resulted in a detectable kidney [1,4-^{13}C$_2$]malate signal early during FA-induced ATN, when only minor histological changes were present, but not in GN. Hyperpolarized [1-^{13}C]pyruvate was not useful in these models, either in diagnosing ATN or in distinguishing tubular necrosis from GN.

Results

Kinetics of Renal Dysfunction and Histological Abnormalities in FA-Induced ATN.
FA-induced ATN resulted in tubular dysfunction (as evidenced by proteinuria) by 10 h (Fig. 1A), although serum urea was normal (Fig. 1B) and there was minimal histological change (Fig. 1C). At 18 h following the induction of ATN, proteinuria worsened (Fig. 1A), serum urea was significantly elevated (Fig. 1B), but histological changes remained relatively minor (Fig. 1 C and F). There was a progressive decline in renal function up to 48 h postinduction of ATN, with worsening histological abnormalities (Fig. 1 A–C and G). This model of ATN, and indeed most murine models of ATN, is limited by the fact that the necrosis observed is more widespread than that typically seen in nephrotoxin-induced ATN in humans. However, necrotic changes in tubules in the FA-induced ATN model used here were largely found to be focal rather than diffuse (i.e., less than 50% of the tubules were involved; Fig. S1). The optimal noninvasive diagnostic test would allow identification of ATN following a rise in urea, when a diagnosis of AKI could be made clinically, but before significant histological damage ensues (at the 18-h time point in this model), optimizing the possible benefits of early therapeutic intervention.

Hyperpolarized [1,4-^{13}C$_2$]Fumarate Detects FA-Induced ATN.
Images acquired following administration of hyperpolarized [1,4-^{13}C$_2$]fumarate demonstrated that both before and 10 h after induction of FA-induced ATN, there was little [1,4-^{13}C$_2$]malate signal in the kidneys (Fig. 2 A and C), whereas by 18 h, a prominent renal [1,4-^{13}C$_2$]malate signal was observed (Fig. 2 A–C). Between 0 and 20 h, the malate/fumarate ratio correlated with the severity of histological changes (Fig. 2D); however, by 26 h, the malate
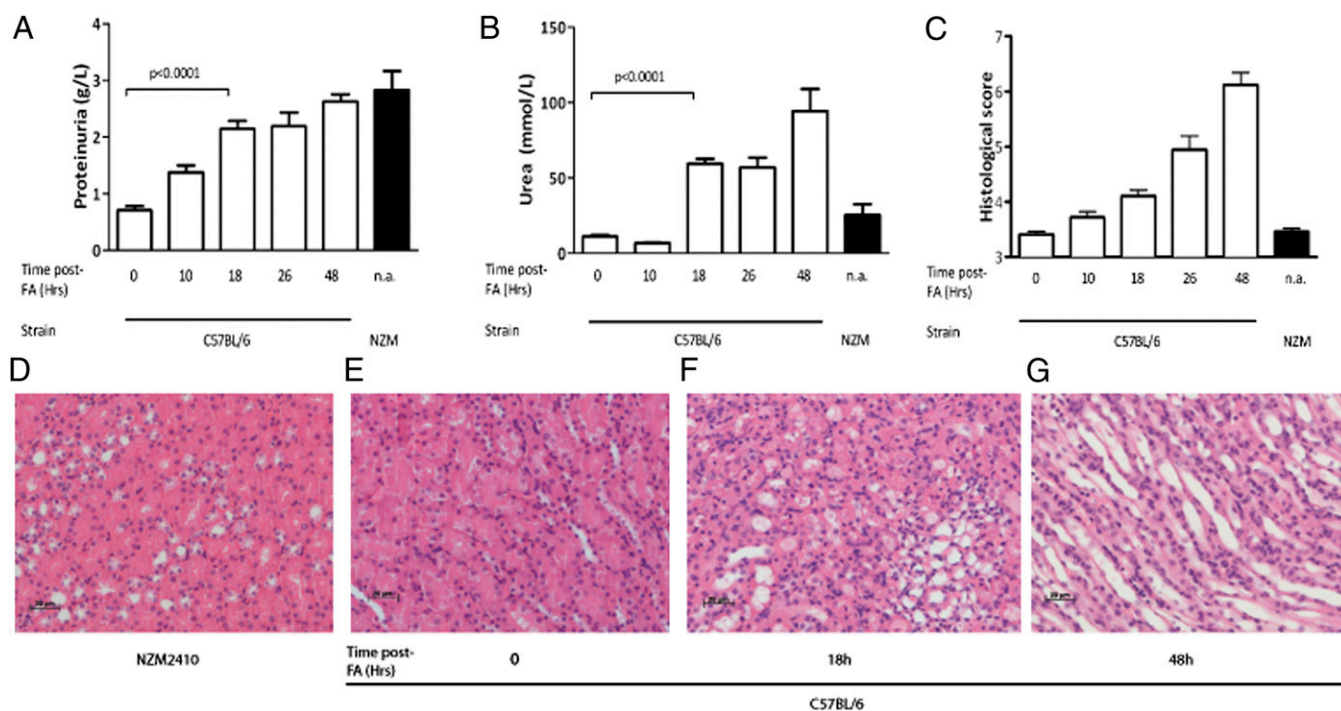

Fig. 1. Clinical and renal histological features. (A–C) Clinical features of renal disease and histopathological severity of ATN were assessed at baseline, and at 10, 18, 26, and 48 h following administration of FA and in NZM2410 mice. Proteinuria (A), serum urea (B), and the score of histological changes (tubular dilatation, cast formation, and necrosis, with a minimum score of 3) (C) are shown. Graphs represent the mean value for at least three mice, and the error bars denote the SEM. Representative images of the corticomedullary junction from H&E-stained kidney sections of untreated mice (D), NZM2410 mice (E), 18 h post-FA (F), and 48 h post-FA (G). (Magnification: D–G, 200×.) n.a., not applicable.
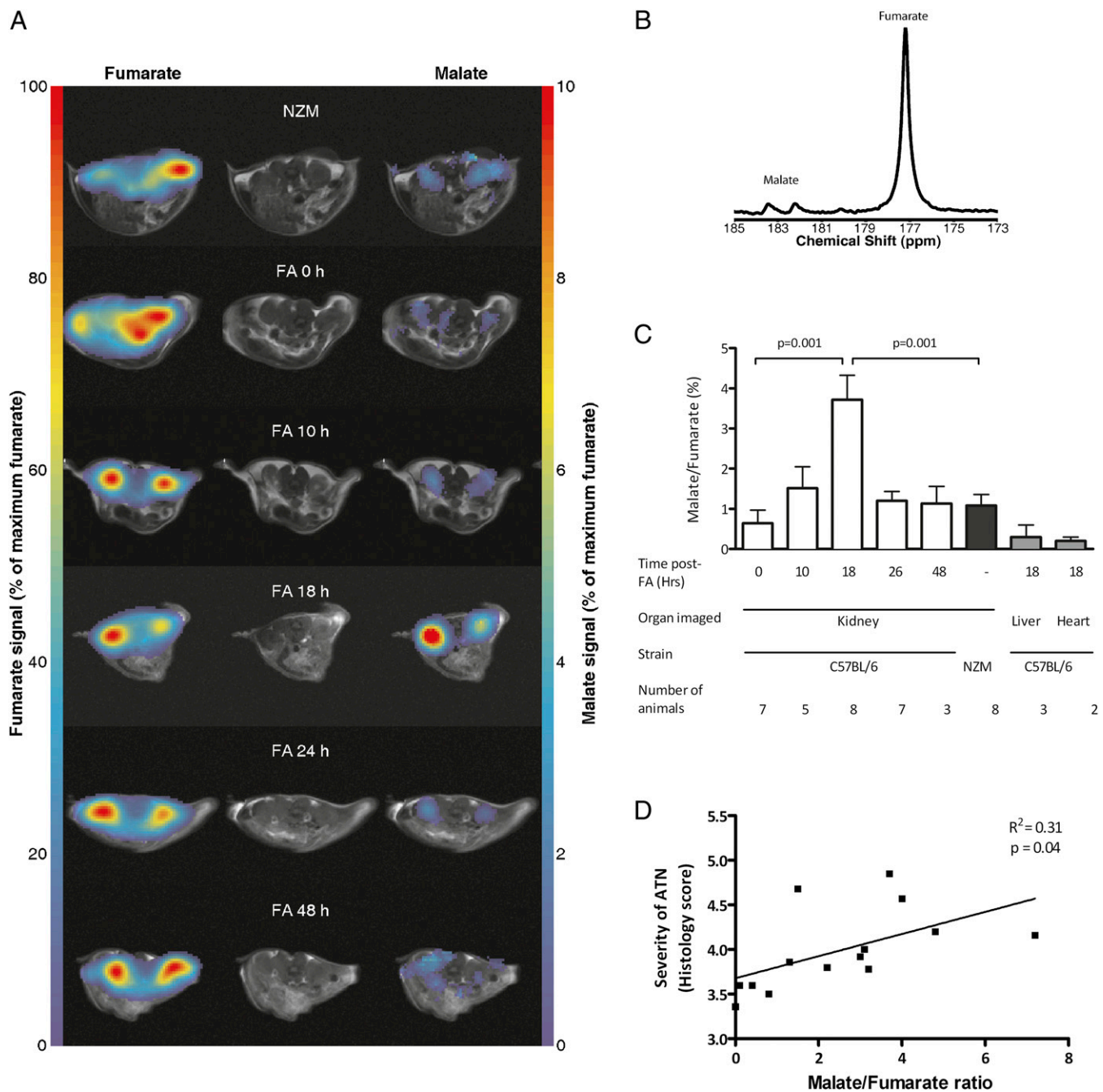
Clatworthy et al.

MEDICAL SCIENCES

Fig. 2. [1,4-^{13}C$_2$]Malate signal was detectable early after the induction of ATN. (*A*) Distribution of normalized [1,4-^{13}C$_2$]fumarate and [1,4-^{13}C$_2$]malate signals following fumarate injection in an NZM2410 mouse and at 0, 10, 18, 24, and 48 h after FA treatment in C57BL/6 mice. Each chemical shift image has been normalized separately to its maximum signal intensity. (*B*) ^{13}C spectrum acquired from slices through the kidney of a mouse with ATN. The signal from hyperpolarized fumarate is at 177.2 ppm, and the signals from [1-^{13}C]malate and [4-^{13}C]malate are at 183.6 ppm and 182.4 ppm, respectively. (*C*) Malate/fumarate ratio in the kidneys, heart, and liver following administration of FA in C57BL/6 and NZM2410 mice, as measured from slice-selective ^{13}C spectra. The values are the mean value of at least three mice (number of mice shown on graph), and the error bars denote the SEM. Similar results were obtained from analysis of CSI data, with the malate/fumarate ratio reaching 6 ± 3% in the kidneys ($n = 7$; $P < 0.01$) at 18 h post-FA treatment. For the times indicated as 18, 26, and 48 h, the data were acquired between 16 and 20 h, 22 and 30 h, and 44 and 54 h, respectively. (*D*) Correlation of histological score and malate/fumarate ratio in mice imaged between 0 and 20 h after induction of ATN.

signal decreased and remained low up to 48 h despite abnormal renal function (Fig. 1 *A* and *B*) and severe histological ATN (Fig. 1 *E–G*). This may be attributable to loss of fumarase from the kidney at later time points, a hypothesis supported by the demonstration of reduced fumarase in necrotic tubules (Fig. S2 *A and B*) and a reduction in total fumarase detectable by Western blotting at 18 and 28 h postinduction of ATN (Fig. S2 *C and D*).

A similar decrease in the levels of fumarase was observed in kidney samples obtained from patients with posttransplant ATN. Fumarase was readily detectable in intact human renal tubular cells but was reduced or absent in tubules disrupted by ATN (Fig. S3), suggesting the potential clinical utility of hyperpolarized [1,4-^{13}C$_2$]fumarate MRS imaging (MRSI) in humans with significant tubular necrosis.

In animals with ATN, the $[1,4\text{-}^{13}C_2]$malate signal was limited to the kidneys, with minimal levels observed in liver and heart (Fig. 2C), suggesting that the malate was generated in the kidneys rather than by renal concentration of malate produced systemically. We determined the specificity of the technique by assessing whether necrosis in an extrarenal site led to $[1,4\text{-}^{13}C_2]$malate signal in the kidneys. In lymphoma tumor-bearing animals 24 h after treatment with etoposide, where the tumor malate/fumarate ratio was $13.4\% \pm 2.4\%$ ($n = 3$), the kidney malate/fumarate ratio was $2.7\% \pm 1.0\%$ ($n = 5$), which was significantly ($P < 0.05$) higher than that observed in non–tumor-bearing, etoposide-treated animals ($0.5 \pm 0.2\%$, $n = 2$). However, in these tumor-bearing mice, there was large-scale necrosis, with 30–40% necrosis in ~1 g of tumor tissue in a mouse weighing 20–25 g.

Hyperpolarized $[1,4\text{-}^{13}C_2]$Fumarate Does Not Detect Lupus Nephritis. To determine if hyperpolarized $[1,4\text{-}^{13}C_2]$fumarate would allow distinction of early ATN from another cause of AKI, we assessed the $[1,4\text{-}^{13}C_2]$malate/fumarate ratio in the kidneys of NZM2410 mice. These mice develop GN secondary to immune complex deposition but have no histological evidence of ATN, as is found in patients with lupus nephritis. Proteinuria is observed at ~6 mo and is followed by a terminal decline in renal function over subsequent weeks. We imaged this murine model of GN following the onset of proteinuria and abnormal renal function. The kidney $[1,4\text{-}^{13}C_2]$malate signal was similar to that observed in mice before FA-induced ATN and was significantly lower than at 18 h post-ATN (Fig. 2 A and C).

Hyperpolarized $[1\text{-}^{13}C]$Pyruvate Does Not Detect ATN or Lupus Nephritis. The kidney $[1\text{-}^{13}C]$pyruvate/$[1\text{-}^{13}C]$lactate ratio showed considerable variability and was not significantly decreased in animals with ATN or increased in animals with GN (Fig. 3).

Discussion

We have demonstrated that imaging the metabolism of hyperpolarized $[1,4\text{-}^{13}C_2]$fumarate in the kidney can be used to detect early tubular necrosis. This important feature could identify a window of opportunity when therapeutic interventions in ATN are more likely to be of use. In our study, the $[1,4\text{-}^{13}C_2]$malate signal became visible at the 18-h time point, when renal function was clearly abnormal. Histopathological changes at this time point were minor, with limited necrosis of tubular cells (Fig. S1). Histopathological studies in humans with ATN are infrequent but show subtle histological changes in patients biopsied, with limited necrosis (4). Our data would suggest that hyperpolarized $[1,4\text{-}^{13}C_2]$fumarate MRSI has the potential to identify damage that results in minimal histological change but is associated with significantly impaired renal function, which is precisely the clinical presentation observed in humans with ATN. One caveat to our findings is that murine models of ATN, including our model, tend to be characterized by more extensive necrosis than that observed in ATN in humans (29). However, a $[1,4\text{-}^{13}C_2]$malate signal was detectable in the presence of focal tubular necrosis (Fig. S1). In addition, more extensive necrosis than this is observed posttransplantation in deceased cardiac death (DCD) donor kidneys, which have more prolonged warm ischemic times (30). Given the increasing use of DCD donor kidneys as a result of organ shortage, our findings are likely to be applicable to this important clinical scenario.

A major diagnostic challenge in patients with AKI is to distinguish ATN from acute GN. We have shown that hyperpolarized $[1,4\text{-}^{13}C_2]$fumarate also allows the distinction of tubular necrosis from glomerular inflammation in the context of renal impairment, adding to its potential clinical utility. The maximum malate/fumarate ratio was observed 16–20 h after induction of ATN. By 48 h, when clinical and histological features of disease were most severe, the ratio had decreased to near-normal levels, which may be explained by the loss of fumarase
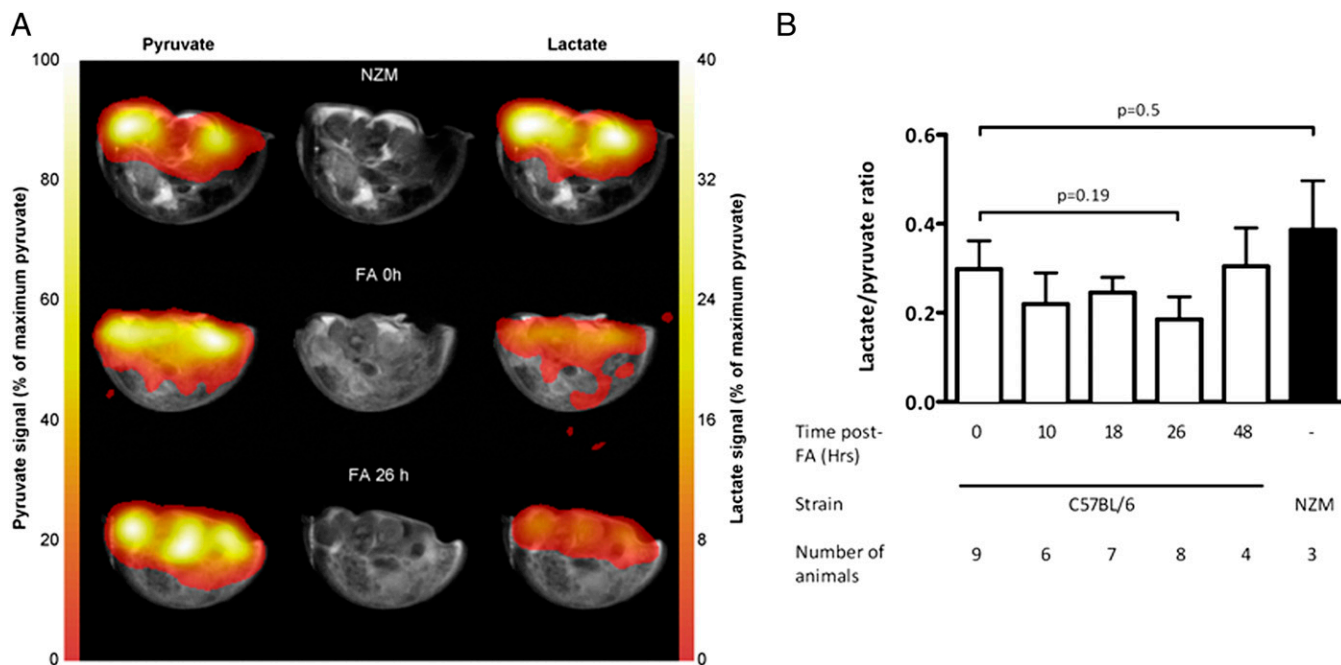

Fig. 3. Hyperpolarized $[1\text{-}^{13}C]$lactate/$[1\text{-}^{13}C]$pyruvate ratio is not changed significantly in the kidneys of FA-treated mice or in NZM2410 mice. (A) Distribution of normalized $[1\text{-}^{13}C]$pyruvate and $[1\text{-}^{13}C]$lactate signals following fumarate injection in an NZM2410 mouse and at 0 and 26 h after FA treatment in C57BL/6 mice. Each chemical shift image has been normalized separately to its maximum signal intensity. (B) Lactate/pyruvate ratio in the kidneys of C57BL/6 mice following the administration of hyperpolarized $[1\text{-}^{13}C]$pyruvate, at the specified times following FA treatment, and in NZM2410 mice, as measured from slice-selective ^{13}C spectra.

Clatworthy et al.

www.manaraa.com

from damaged tubular cells, which was observed at later time points. A similar loss of fumarase was observed from renal tubules in human kidneys affected by ATN, which supports the potential of the hyperpolarized [1,4-^{13}C$_2$]fumarate experiment for diagnosing ATN in the clinic. AKI has a number of differential diagnoses in addition to acute GN, such as tubulointerstitial nephritis. Careful kinetic and histopathological studies of these diagnoses will need to be performed alongside those for ATN and acute GN to define the clinical role of this imaging modality in humans.

Our studies in tumor-bearing, etoposide-treated animals suggest that [1,4-^{13}C$_2$]malate generated by necrotic cells extrarenally may be transported to the kidneys, resulting in a detectable malate signal within the kidney. This represents a potential limitation of this imaging technique if used in patients with significant necrosis in nonrenal tissues. However, although malate was detectable in the kidneys of tumor-bearing, etoposide-treated animals, the malate/fumarate ratio was still significantly lower than that observed in kidneys with ATN. Moreover, the etoposide-treated tumor model results in massive, synchronized necrosis (as evidenced by the profound elevation of the fumarate/malate ratio observed in these tumors). Such levels of necrosis are unlikely to occur outside of this context.

Hyperpolarized [1-^{13}C]pyruvate has been used previously to assess chemotherapy-induced tumor necrosis (21, 23, 31, 32). A decrease in lactate labeling in drug-treated tumors reflected a number of factors, including loss of LDH and NADH and a decrease in tumor lactate concentration. In patients with ATN, LDH lost from tubular cells is detectable in the urine (24, 25), which raised the possibility that a reduction in hyperpolarized [1-^{13}C]lactate signal may occur in ATN. Indeed, we did see a trend toward a reduction in lactate/pyruvate ratio up to 26 h postadministration of FA, but this did not reach statistical significance because of the wide variability in the values obtained. This variability likely reflects the fact that the rate of ^{13}C label exchange between [1-^{13}C]pyruvate and endogenous lactate is dependent on a number of factors, including the rate of pyruvate delivery to the tissue, the lactate concentration, and the activity of LDH, and these factors may change in opposite directions in ATN. In ATN, secondary to both ischemia-reperfusion and toxin injury, tubular cells become hypoxic (33). LDH is one of the genes up-regulated by hypoxia-inducible factor-1α (34), a transcription factor known to be increased in ATN (35, 36). The increase in LDH activity, coupled with the expected increase in lactate concentration in the hypoxic tissue, will increase the degree of lactate labeling (37). The hyperpolarized [1-^{13}C]lactate signal obtained from the kidney will reflect the summed value of the increased labeled lactate labeling generated in intact, hypoxic tubular cells and the decrease attributable to loss of LDH, lactate, and NADH from frankly necrotic tubular cells. Thus, if these two processes are both increased in ATN, the net measurable [1-^{13}C]lactate signal may not change significantly. In contrast, one of the advantages of imaging hyperpolarized [1,4-^{13}C$_2$]fumarate is that it appears to provide an unequivocal indication of the cell damage that results in loss of membrane integrity. In healthy cells, there is little or no detectable uptake of hyperpolarized [1,4-^{13}C$_2$]fumarate within the lifetime of polarization. However, in damaged cells, where plasma membrane permeability is compromised, there is rapid uptake of labeled fumarate and conversion to hyperpolarized [1,4-^{13}C$_2$]malate.

In conclusion, we have demonstrated that imaging the conversion of hyperpolarized [1,4-^{13}C$_2$]fumarate into malate in the kidney can contribute to early diagnosis of tubular necrosis and allows its distinction from acute GN. Although the malate signal was detectable for only a limited period, it nevertheless may allow identification of a window of opportunity for therapeutic intervention before the onset of significant histological change. These data, together with the ongoing clinical trial of hyper-

polarized ^{13}C MRSI in prostate cancer (ClinicalTrials.gov Identifier: NCT01229618), support the potential of hyperpolarized [1,4-^{13}C$_2$]fumarate MRS in contributing to the diagnosis of ATN in the clinic.

Materials and Methods

Animals. C57BL/6 mice (aged 10–16 wk; Charles River Laboratories) and NZM2410 mice (aged 6–9 mo) were used. For FA-induced ATN, 250 mg/kg of FA (Sigma–Aldrich) dissolved in 150 mM sodium bicarbonate was administered i.p.. All procedures were conducted in accordance with the UK Animals (Scientific Procedures) Act 1986. Experiments with tumors were designed with reference to the UK Coordinating Committee on Cancer Research Guidelines for the Welfare of Animals in Experimental Neoplasia. The work was approved by the Cambridge University Ethical Review Panel and the Licence Review Committee.

MRSI. Animals were anesthetized with i.p. Hypnorm (VetaPharma)/Hypnovel (Roche)/dextrose-saline (4%:0.18%, wt/vol) in a 5:4:31 ratio (10 mL/kg of body weight). Hyperpolarized [1,4-^{13}C$_2$]fumarate was prepared as described previously (22). Briefly, [1,4-^{13}C$_2$]fumaric acid (3.23 mmol; Cambridge Isotope Laboratories, Inc.) was dissolved in 8.74 mmol of DMSO containing 11.48 μmol of a trityl radical (~18.5 mM, AH111501; GE Healthcare) and 0.48 μmol of a gadolinium chelate [~0.8 mM, Gd-3; GE Healthcare (38)]. The solution was sonicated and centrifuged, and a 40-mg aliquot was hyperpolarized as described (22). The sample was then dissolved in 6 mL of buffer containing 40 mM phosphate, 50 mM sodium chloride, and 40 mM sodium hydroxide (pH 7.4) that had been pressurized to 10 bar and was at 180 °C. [1-^{13}C] pyruvic acid samples (44 mg, 14 M, 91% ^{13}C) contained 15 mM trityl radical (OX063; GE Healthcare) and 1.4 mM gadolinium chelate (ProHance; Bracco International B.V.). Following hyperpolarization, the sample was dissolved rapidly in 6 mL of Hepes buffer (40 mM Hepes, 94 mM NaOH, 30 mM NaCl, and 100 mg/L EDTA) pressurized to 10 bar and at 180 °C (21). The final concentration of [1-^{13}C]pyruvate was 75 mM. The dissolved solutions containing 20 mM [1,4-^{13}C$_2$]fumarate or 75 mM [1-^{13}C]pyruvate were cooled to ~37 °C before i.v. injection. All chemicals were obtained from Sigma–Aldrich, unless stated otherwise.

MRI experiments were performed in a 9.4-T, vertical, wide-bore (8.9 cm) magnet (Oxford Instruments) equipped with actively shielded gradients (Magnex) interfaced to a Varian ^{UNITY}INOVA console (Varian, Inc.). A surface coil (diameter of 24 mm) tuned to 100 MHz was located over the kidneys, and the animal holder was placed inside a volume coil (Millipede; Varian, Inc.) tuned to 400 MHz. In some FA-treated animals (16–20 h, n = 3), the surface coil was placed over the liver. Transverse ^{1}H images were acquired using a spin-echo pulse sequence [repetition time (TR), 1.5 s; echo time (TE), 30 ms; field of view, 32 mm × 32 mm; data matrix, 256 × 128; slice thickness, 2 mm; 11 slices], and an 8-mm transverse slice through the kidneys was selected. ^{13}C data collection was started 20 s after the beginning of a 2-s i.v. injection of 200 μL [1,4-^{13}C$_2$]fumarate or [1-^{13}C]pyruvate. A single ^{13}C spectrum was first collected from the whole slice using a 600-μs sinc pulse with a nominal flip angle of 5° (TE, 2 ms; spectral width, 8,000 Hz collected into 768 complex data points), and this was immediately followed by chemical shift imaging (CSI), with phase-encoding gradients added to the pulse sequence (TE, 2 ms; TR, 20 ms; spectral width, 8,000 Hz collected into 136 complex data points; field of view, 40 × 40 mm^2; data matrix, 16 × 16). Peak integrals for fumarate, malate, pyruvate, and lactate were calculated in MATLAB (MathWorks) from phase- and baseline-corrected spectra in each voxel to generate metabolite maps, which were overlaid on reference proton images. Before analysis, data were spatially smoothed with a Gaussian filter and zero-filled to 128 × 128 to match the size of reference image. Malate/fumarate and lactate/pyruvate ratios were calculated from pulse-acquired spectra and from CSI data in regions of interest covering the kidneys.

Murine Renal Histology. Three or more FA-treated animals were killed at each time point for histological analysis. Kidneys were fixed in formalin and embedded in paraffin. Sections (7 μm) were stained with H&E. All analyses were performed blinded to sample identity. Tubulointerstitial damage was assessed by scoring three parameters; tubular necrosis, tubular dilatation, and cast formation. Scores were as follows: involvement of 0–25% of tubules within each cortical or medullary high-powered field (HPF), 1; 25–50%, 2; 50–75%, 3; and 75–100%, 4. Fifteen randomly chosen, nonoverlapping fields (400× magnification) were scored in each kidney section.

www.manaraa.com

Serum Urea Measurement. Serum urea was measured using a urease assay (Dade Behring, distributed by Siemens Healthcare) and a Siemens Dimension RxL analyzer as detailed by Burtis and Ashwood (39).

Human Kidney Samples. Experiments using human tissue were performed with informed consent and approval of the Cambridge Local Research Ethical Committee and Cambridge University Hospitals Tissue Bank. Renal tissue was obtained from allograft biopsies with posttransplant ATN (confirmed by a clinical histopathologist). Tissue was placed in CRYO-M-BED embedding compound (Bright Instrument Co. Ltd.) and snap-frozen in liquid nitrogen.
Immunofluorescence. Murine kidneys were obtained from vehicle-treated and FA-treated animals, and snap-frozen in ornithine carbamoyltransferase. Sections (30 μm) were blocked for 1–2 h and subsequently stained with a polyclonal rabbit anti-mouse–fumarase antibody (Novus Biologicals) or normal rabbit serum. A phycoerythrin-labeled secondary antibody was used. Alexa-Fluor647-conjugated phalloidin (Invitrogen Molecular Probes) was used to stain actin, and Hoechst (Invitrogen Molecular Probes) was used to stain nuclei. Images were obtained on a Zeiss LSM 710 microscope (Carl Zeiss Microimaging) using a 20× objective, and scale bars added using Imaris software (Bitplane).

Human kidney sections were obtained from biopsy samples with confirmed posttransplant ATN (diagnosed by a clinical pathologist). Ten-micrometer sections were blocked with normal goat serum in 0.1 M Tris and 0.1% Triton-X (Sigma) for 1–2 h and subsequently stained with a mouse antifumarase monoclonal antibody or an isotype control followed by a goat anti-mouse AlexaFluor568-conjugated secondary. AlexaFluor647-conjugated phalloidin was used to stain actin, and Hoechst was used to stain nuclei. Phalloidin, Hoechst, and all antibodies used were obtained from Invitrogen Molecular Probes. Sections were mounted in Vectashield Mounting Medium (Vector Laboratories). Images were obtained on a Zeiss LSM 510 microscope (Carl Zeiss Microimaging) using a 40× objective, and scale bars were added using Improvision Volocity Software (Perkin- Elmer).
Western blotting. A rabbit antifumarase antibody (Novus Biologicals) was used in a standard Western blotting protocol.

Statistical Methods. Statistical analyses of proteinuria, urea, and histological score (Student's *t* test) were performed using GraphPad Prism.

1. Nash K, Hafeez A, Hou S (2002) Hospital-acquired renal insufficiency. *Am J Kidney Dis* 39:930–936.
2. Brivet FG, Kleinknecht DJ, Loirat P, Landais PJ; French Study Group on Acute Renal Failure (1996) Acute renal failure in intensive care units—Causes, outcome, and prognostic factors of hospital mortality; A prospective, multicenter study. *Crit Care Med* 24:192–198.
3. Thadhani R, Pascual M, Bonventre JV (1996) Acute renal failure. *N Engl J Med* 334:1448–1460.
4. Solez K, Morel-Maroger L, Sraer JD (1979) The morphology of "acute tubular necrosis" in man: Analysis of 57 renal biopsies and a comparison with the glycerol model. *Medicine (Baltimore)* 58:362–376.
5. Venkatachalam MA, Bernard DB, Donohoe JF, Levinsky NG (1978) Ischemic damage and repair in the rat proximal tubule: Differences among the S1, S2, and S3 segments. *Kidney Int* 14:31–49.
6. Diamond JR, Yoburn DC (1982) Nonoliguric acute renal failure associated with a low fractional excretion of sodium. *Ann Intern Med* 96:597–600.
7. Manno C, et al. (2004) Predictors of bleeding complications in percutaneous ultrasound-guided renal biopsy. *Kidney Int* 66:1570–1577.
8. Whittier WL, Korbet SM (2004) Timing of complications in percutaneous renal biopsy. *J Am Soc Nephrol* 15:142–147.
9. Chatterjee PK, et al. (2004) Differential effects of caspase inhibitors on the renal dysfunction and injury caused by ischemia-reperfusion of the rat kidney. *Eur J Pharmacol* 503(1-3):173–183.
10. Sharfuddin AA, et al. (2009) Soluble thrombomodulin protects ischemic kidneys. *J Am Soc Nephrol* 20:524–534.
11. Kunzendorf U, Haase M, Rölver L, Haase-Fielitz A (2010) Novel aspects of pharmacological therapies for acute renal failure. *Drugs* 70:1099–1114.
12. Bellomo R, Ronco C, Kellum JA, Mehta RL, Palevsky P; Acute Dialysis Quality Initiative workgroup (2004) Acute renal failure—Definition, outcome measures, animal models, fluid therapy and information technology needs: The Second International Consensus Conference of the Acute Dialysis Quality Initiative (ADQI) Group. *Crit Care* 8:R204–R212.
13. Mehta RL, et al.; Acute Kidney Injury Network (2007) Acute Kidney Injury Network: Report of an initiative to improve outcomes in acute kidney injury. *Crit Care* 11:R31.
14. Mishra J, et al. (2005) Neutrophil gelatinase-associated lipocalin (NGAL) as a biomarker for acute renal injury after cardiac surgery. *Lancet* 365:1231–1238.
15. Haase M, Bellomo R, Devarajan P, Schlattmann P, Haase-Fielitz A; NGAL Meta-analysis Investigator Group (2009) Accuracy of neutrophil gelatinase-associated lipocalin (NGAL) in diagnosis and prognosis in acute kidney injury: A systematic review and meta-analysis. *Am J Kidney Dis* 54:1012–1024.
16. Thoeny HC, De Keyzer F (2011) Diffusion-weighted MR imaging of native and transplanted kidneys. *Radiology* 259:25–38.
17. Tugnoli V, et al. (2003) 1H-NMR and 13C-NMR lipid profiles of human renal tissues. *Biopolymers* 72:86–95.
18. Radda GK (1986) The use of NMR spectroscopy for the understanding of disease. *Science* 233:640–645.
19. Ardenkjaer-Larsen JH, et al. (2003) Increase in signal-to-noise ratio of > 10,000 times in liquid-state NMR. *Proc Natl Acad Sci USA* 100:10158–10163.
20. Gallagher F, Kettunen M, Brindle K (2009) Biomedical applications of hyperpolarized ^{13}C magnetic resonance imaging. *Prog Nucl Magn Reson Spectrosc* 55:285–295.

21. Day SE, et al. (2007) Detecting tumor response to treatment using hyperpolarized ^{13}C magnetic resonance imaging and spectroscopy. *Nat Med* 13:1382–1387.
22. Gallagher FA, et al. (2009) Production of hyperpolarized [1,4-$^{13}C_2$]malate from [1,4-$^{13}C_2$]fumarate is a marker of cell necrosis and treatment response in tumors. *Proc Natl Acad Sci USA* 106:19801–19806.
23. Witney TH, et al. (2010) Detecting treatment response in a model of human breast adenocarcinoma using hyperpolarised [1-^{13}C]pyruvate and [1,4-$^{13}C_2$]fumarate. *Br J Cancer* 103:1400–1406.
24. Westhuyzen J, et al. (2003) Measurement of tubular enzymuria facilitates early detection of acute renal impairment in the intensive care unit. *Nephrol Dial Transplant* 18:543–551.
25. Herget-Rosenthal S, et al. (2004) Prognostic value of tubular proteinuria and enzymuria in nonoliguric acute tubular necrosis. *Clin Chem* 50:552–558.
26. MacKenzie JD, et al. (2011) Detection of inflammatory arthritis by using hyperpolarized 13C-pyruvate with MR imaging and spectroscopy. *Radiology* 259:414–420.
27. Zimmermann HD, Maykemper B, Dieker P (1977) Intra- and extrarenal vascular changes in the acute renal failure of the rat caused by high-dose folic acid injection. *Virchows Arch A Pathol Anat Histol* 376:47–73.
28. Morel L, Rudofsky UH, Longmate JA, Schiffenbauer J, Wakeland EK (1994) Polygenic control of susceptibility to murine systemic lupus erythematosus. *Immunity* 1:219–229.
29. Lieberthal W, Nigam SK (2000) Acute renal failure. II. Experimental models of acute renal failure: Imperfect but indispensable. *Am J Physiol Renal Physiol* 278:F1–F12.
30. Sulikowski T, et al. (2010) Histopathologic evaluation of pretransplantation biopsy as a factor influencing graft function after kidney transplantation in 3-year observation. *Transplant Proc* 42:3375–3381.
31. Bohndiek SE, et al. (2010) Detection of tumor response to a vascular disrupting agent by hyperpolarized 13C magnetic resonance spectroscopy. *Mol Cancer Ther* 9:3278–3288.
32. Day SE, et al. (2011) Detecting response of rat C6 glioma tumors to radiotherapy using hyperpolarized [1-^{13}C]pyruvate and ^{13}C magnetic resonance spectroscopic imaging. *Magn Reson Med* 65:557–563.
33. Weidemann A, et al. (2008) HIF activation protects from acute kidney injury. *J Am Soc Nephrol* 19:486–494.
34. Calvert JW, Cahill J, Yamaguchi-Okada M, Zhang JH (2006) Oxygen treatment after experimental hypoxia-ischemia in neonatal rats alters the expression of HIF-1alpha and its downstream target genes. *J Appl Physiol* 101:853–865.
35. Rosenberger C, et al. (2002) Expression of hypoxia-inducible factor-1alpha and -2alpha in hypoxic and ischemic rat kidneys. *J Am Soc Nephrol* 13:1721–1732.
36. Rosenberger C, et al. (2005) Up-regulation of HIF in experimental acute renal failure: Evidence for a protective transcriptional response to hypoxia. *Kidney Int* 67:531–542.
37. Witney TH, Kettunen MI, Brindle KM (2011) Kinetic modeling of hyperpolarized ^{13}C label exchange between pyruvate and lactate in tumor cells. *J Biol Chem* 286:24572–24580.
38. Gallagher FA, et al. (2008) Magnetic resonance imaging of pH in vivo using hyperpolarized 13C-labelled bicarbonate. *Nature* 453:940–943.
39. Burtis C, Ashwood E (2001) *Fundamentals of Clinical Chemistry* (Saunders, Philadelphia), 5th Ed.

MEDICAL SCIENCES

Clatworthy et al.

www.manaraa.com